Multicolor structured illumination microscopy and quantitative control of polychromatic light with a digital micromirror device: supplement

PETER T. BROWN,[1] RORY KRUITHOFF,[1] GREGORY J. SEEDORF,[2] AND DOUGLAS P. SHEPHERD[1,*]

[1] *Department of Physics and Center for Biological Physics, Arizona State University, Tempe, AZ 85287, USA*
[2] *Department of Pediatrics and Pediatric Heart Lung Center, University of Colorado Anschutz Medical Campus, Aurora, CO 80045, USA*
*douglas.shepherd@asu.edu

Multicolor structured illumination microscopy and quantitative control of polychromatic light with a digital micromirror device: supplemental document

CONTENTS

1. COMPARISON OF COHERENT AND INCOHERENT-PROJECTION SIM

Sinusoidal SIM using a DMD and *incoherent* projection has previously been realized [1], but while this technique has the same theoretical resolution as coherent SIM, its resolution in the presence of noise degrades much more rapidly. The achievable signal in incoherent projection SIM is smaller than coherent SIM by a factor of the optical transfer function at the SIM frequency, $H(\mathbf{f}_o)$. Because the experimental resolution limit of SIM is set by the signal-to-noise ratio (SNR) in the image, coherent SIM has a tremendous advantage over incoherent projection techniques. Achieving comparable results with incoherent projection SIM requires at least one order of magnitude more optical power for realistic SIM frequencies, making it much less efficient with its photon budget and leading to higher photobleaching and phototoxicity.
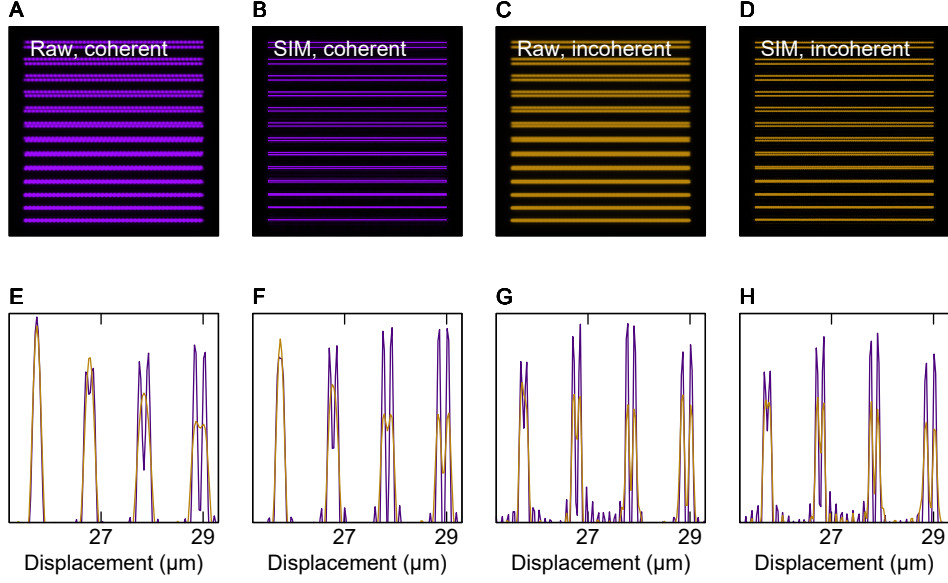
Fig. S1. Comparison of coherent and incoherent SIM versus SNR. A. Simulated raw image for one angle and phase combination using coherent SIM. The moiré pattern features are clearly visible. The SNR in this image is the same as in G. **B**. Reconstructed SIM image corresponding to the raw data in A. **C**. Simulated raw image for one angle and phase combination using incoherent SIM. The moiré pattern is too weak to be seen by eye. The SNR in this images is the same as in G. **D**. Reconstructed SIM image corresponding to the raw data in C. **E**. Line cut illustrating coherent (magenta) and incoherent (yellow) SIM for fixed net intensity at the sample and SNR ∼30, corresponding to peak photon number of ∼1000 photons per pixel. Lines with spacings ranging from 90 nm to 180 nm are shown. At this SNR, the largest three line pairs are resolved by coherent SIM, but not by incoherent SIM. **F**. SNR ∼100. Coherent SIM clearly resolves the first three peaks. Incoherent SIM resolves the first peak, but with worse contrast that coherent SIM. **G**. SNR ∼300. Coherent SIM resolves all four peaks, while incoherent SIM resolves only the first three but with significantly less contrast. **H**. SNR ∼1000. Despite increased signal to noise, the reconstructed SIM images are similar to G. Increasing signal to noise further has only a marginal effect.

Coherent SIM relies on interfering two beams which pass near the edge of the objective pupil. Assuming an ideal optical transfer function, these beams are not attenuated by the OTF, leading to a sinusoidal intensity pattern with full contrast ($m = 1$),

$$I_c^{\text{sample}} \quad = \quad I_o \left[1 + \cos \left(2\pi \mathbf{f}_o \cdot \mathbf{r} + \phi \right) \right]. \tag{S1}$$

Incoherent SIM, on the other hand, relies on forming an image of a sinusoidal *intensity pattern*, and the strength of the modulation is degraded by the optical transfer function

$$I_i^{\text{sample}} \quad = \quad I_o \left[1 + H(\mathbf{f}_o) \cos \left(2\pi \mathbf{f}_o \cdot \mathbf{r} + \phi \right) \right], \tag{S2}$$

implying the modulation depth can be at most $m = H(\mathbf{f}_o)$.

The practical resolution of a SIM measurement is set by the SNR, and the strength of the signal containing superresolution information is determined by $I_o m$. For fixed intensity I_o, achieving the same $I_o m$ value requires a factor of $1/H(\mathbf{f}_o)$ power in the incoherent case. This lower efficiency also leads to enhanced photobleaching and phototoxicity.

Assuming an ideal optical transfer function, setting the SIM pattern at 80 % of the band pass limits the incoherent projection $m < 0.1$. Increasing the SIM frequency further to achieve the full SIM theoretical resolution limit causes the modulation to rapidly deteriorate. Setting the SIM pattern at 95 % of the band pass limits $m < 0.01$, implying that coherent SIM can achieve SNR's a factor of $100\times$ larger than with an equivalent incoherent system. This value is similar to that

chosen in [2], an experiment that would not have been possible using an incoherent projection SIM.

These numbers provide a lower bound on the SNR advantage coherent SIM has over incoherent projection because experimental optical transfer functions typically decay faster than the ideal OTF. The experimental OTF we obtained in section 3.1 implies $m < 0.02$ and 0.002 at 80 % and 95 % of the theoretical band pass, respectively.

To illustrate the effect this difference has on the image quality, we simulated SIM raw images and reconstructions of the same line pairs discussed in Supplemental Note 13. We summarize the results in Fig. S1. We find that coherent SIM resolves smaller line pairs and thus achieves significantly better resolution than incoherent SIM at all SNR values we consider (Fig. S1E-H). As expected, the weaker modulation in the incoherent case leads to a visibly weaker moiré pattern in the raw SIM images (Fig. S1A,C).

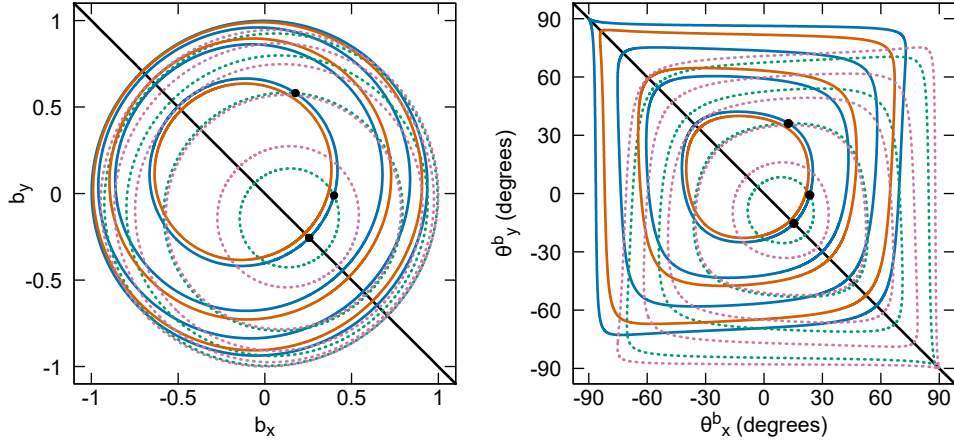## 2. GENERAL CLOSED-FORM SOLUTION OF THE BLAZE AND DIFFRACTION CONDITIONS

Fig. S2. Blaze and diffraction condition solution contours. A. Output diffraction angles parameterized by the unit vector components b_x and b_y for "on" mirrors and 465 nm for $n = 1, ..., 4$ (blue) and 635 nm for $n = 1, ..., 3$ (red), and solutions for "off" mirrors and 532 nm for $n = -4, ..., -1$ (green) and 405 nm for $n = -5, ..., -1$ (purple). The shapes with smaller radii correspond to the higher diffraction orders. The black line indicates the $\theta_x = -\theta_y$ direction, and the black dots indicate the 3- and 4-color solutions discussed in the text. **B**. Diffraction output angle data from A. parameterized by θ_x and θ_y.

Here we present a closed form solution to the combined blaze and diffraction problem, which removes any need to perform numerical simulations to determine appropriate input/output angles and diffraction orders for determining optimal points for multicolor operation. Further, it allows us to answer various useful questions which have not previously been addressed, including which diffraction orders can be overlapped with the blaze condition in principle.

To find a joint solution to the blaze and diffraction conditions, it is convenient to work directly with the incoming and outgoing unit vectors $\hat{\mathbf{a}}$ and $\hat{\mathbf{b}}$ as opposed to parameterizing these by angles, which corresponds to working with the direction cosines [3]. However, for later convenience we also introduce an angular parameterization following [4],

$$\hat{\mathbf{a}} = \left(\tan \theta_n^a \hat{\mathbf{n}} + \tan \theta_{n_\perp}^a \hat{\mathbf{n}}_\perp + \hat{\mathbf{z}} \right) / \sqrt{\tan^2 \theta_n^a + \tan^2 \theta_{n_\perp}^a + 1} \tag{S3}$$

$$\hat{\mathbf{b}} = \left(\tan \theta_n^b \hat{\mathbf{n}} + \tan \theta_{n_\perp}^b \hat{\mathbf{n}}_\perp - \hat{\mathbf{z}} \right) / \sqrt{\tan^2 \theta_n^b + \tan^2 \theta_{n_\perp}^b + 1} \tag{S4}$$

where we most often consider the bases $\hat{\mathbf{n}}, \hat{\mathbf{n}}_\perp = \hat{\mathbf{x}}, \hat{\mathbf{y}}$ and $\hat{\mathbf{n}}, \hat{\mathbf{n}}_\perp = (\hat{\mathbf{x}} - \hat{\mathbf{y}}) / \sqrt{2}, (\hat{\mathbf{x}} + \hat{\mathbf{y}}) / \sqrt{2}$. θ_n is the angle between the $\hat{\mathbf{n}}$ axis and the unit vector $\hat{\mathbf{a}}$ or $\hat{\mathbf{b}}$ projected onto the $\hat{\mathbf{n}}_\perp - \hat{\mathbf{z}}$ plane.

Now, we exploit the fact that the blaze condition is synonymous with the law of reflection being satisfied on a single micromirror. To more easily evaluate this condition, we adopt the basis

$$\hat{\mathbf{e}}_1 = \frac{1}{\sqrt{2}}(\hat{\mathbf{x}} - \hat{\mathbf{y}})\cos\gamma - \hat{\mathbf{z}}\sin\gamma \tag{S5}$$

$$\hat{\mathbf{e}}_2 = \frac{1}{\sqrt{2}}(\hat{\mathbf{x}} + \hat{\mathbf{y}}) \tag{S6}$$

$$\hat{\mathbf{e}}_3 = \frac{1}{\sqrt{2}}(\hat{\mathbf{x}} - \hat{\mathbf{y}})\sin\gamma + \hat{\mathbf{z}}\cos\gamma, \tag{S7}$$

which is chosen such that $\hat{\mathbf{e}}_3$ is the micromirror normal. In this basis, the blaze condition is

$$a_1 - b_1 = 0 \tag{S8}$$
$$a_2 - b_2 = 0 \tag{S9}$$
$$a_3 + b_3 = 0, \tag{S10}$$

which is equivalent to $A_\pm(\gamma, \hat{\mathbf{a}} - \hat{\mathbf{b}}) = 0$.

The general diffraction condition occurs when the exponentials in eq. 1 of the main text all enter with the same phase, and can be written

$$a_x - b_x = \frac{\lambda}{d}n_x \tag{S11}$$

$$a_y - b_y = \frac{\lambda}{d}n_y, \tag{S12}$$

which in the new basis becomes

$$(a_1 - b_1)\frac{\cos\gamma}{\sqrt{2}} + (a_2 - b_2)\frac{1}{\sqrt{2}} + (a_3 - b_3)\frac{\sin\gamma}{\sqrt{2}} = \frac{\lambda}{d}n_x \tag{S13}$$

$$-(a_1 - b_1)\frac{\cos\gamma}{\sqrt{2}} + (a_2 - b_2)\frac{1}{\sqrt{2}} - (a_3 - b_3)\frac{\sin\gamma}{\sqrt{2}} = \frac{\lambda}{d}n_y. \tag{S14}$$

Adding and subtracting these two equations, we find

$$a_2 - b_2 = \frac{\lambda}{\sqrt{2}d}(n_x + n_y) \tag{S15}$$

$$(a_2 - b_2)\cos\gamma + (a_3 - b_3)\sin\gamma = \frac{\lambda}{\sqrt{2}d}(n_x - n_y) \tag{S16}$$

Inserting eqs. S8–S10, we find that the blaze condition and diffraction conditions can only be satisfied together for $n = n_x = -n_y$, and in this case

$$a_3 = \frac{1}{\sqrt{2}\sin\gamma}\frac{\lambda}{d}n \tag{S17}$$

$$a_2 = \pm\sqrt{1 - a_3^2 - a_1^2} \tag{S18}$$

$$a_1 \in \left[-\sqrt{1 - a_3^2}, \sqrt{1 - a_3^2}\right], \tag{S19}$$

and two numbers, n and a_1 completely specify the solution. Further the condition $0 < a_3 \leq 1$ implies this equation can only be satisfied for a finite number of n,

$$n = \begin{cases} 1, ..., \lfloor \frac{d}{\lambda}\sqrt{2}\sin\gamma \rfloor & \text{if } \gamma < 0 \\ \lceil -\frac{d}{\lambda}\sqrt{2}\sin\gamma \rceil, ..., -1 & \text{if } \gamma > 0, \end{cases} \tag{S20}$$

where $\lfloor \cdot \rfloor$ and $\lceil \cdot \rceil$ are the floor and ceiling functions respectively.

For any solution, we can convert eqs. S17–S19 back to the $\hat{\mathbf{x}}$, $\hat{\mathbf{y}}$, $\hat{\mathbf{z}}$ basis using eqs. S5–S7. We explicitly perform this substitution for the case of most interest, $a_x = -a_y$ ($\theta_x = -\theta_y$), which implies $a_2 = 0$. Therefore,

4

$$\hat{\mathbf{a}} = \frac{\hat{\mathbf{x}} - \hat{\mathbf{y}}}{\sqrt{2}} \sin(\alpha + \gamma) + \hat{\mathbf{z}} \cos(\alpha + \gamma) \tag{S21}$$

$$\hat{\mathbf{b}} = \frac{\hat{\mathbf{x}} - \hat{\mathbf{y}}}{\sqrt{2}} \sin(\alpha - \gamma) - \hat{\mathbf{z}} \cos(\alpha - \gamma) \tag{S22}$$

where

$$\cos \alpha = \frac{1}{\sqrt{2} \sin \gamma} \frac{\lambda}{d} n \tag{S23}$$

or, writing in terms of the parameterization eq. S3–S4 for $(\hat{\mathbf{x}} - \hat{\mathbf{y}})/\sqrt{2}$, $(\hat{\mathbf{x}} + \hat{\mathbf{y}})/\sqrt{2}$, $\hat{\mathbf{z}}$,

$$\theta_{x-y}^a = \alpha + \gamma \tag{S24}$$

$$\theta_{x-y}^b = \alpha - \gamma, \tag{S25}$$

which gives *two* explicit solutions for the input and output angles in terms of only n and γ, one for each solution to eq. S23.

For multicolor operation, we must solve eqs. S17–S19 for multiple wavelengths, $\lambda_1, ..., \lambda_n$ subject to the condition $\hat{\mathbf{b}}_1 = \hat{\mathbf{b}}_2 = ... = \hat{\mathbf{b}}_n$. We see from these equations that for fixed value of γ this requires $\lambda_1 n_1 = ... = \lambda_n n_n$, which can be solved using the algorithm described in the main text. The only continuously tuneable parameters here are the wavelengths, which is undesirable because wavelength choices will often be dictated by choice of fluorophore, existing equipment, or available laser sources.

On the other hand, we can generically find a solution for two colors using the "on" and "off" mirror states of the DMD by tuning the input angles. In this case, let the wavelength and diffraction order for the "on" ("off") mirrors be λ_p and n_p (λ_m and n_m). Suppose $\gamma = \gamma_{\text{on}} = -\gamma_{\text{off}}$. Then $\hat{\mathbf{b}}_p = \hat{\mathbf{b}}_m$ gives the quadratic equation

$$b_z = \frac{1}{2\sqrt{2} \sin \gamma \cos \gamma} \frac{-\lambda_p n_p + \lambda_m n_m}{d} \tag{S26}$$

$$b_x^2 + b_x \left(\frac{\lambda_p n_p + \lambda_m n_m}{2 \sin^2 \gamma d} \right) = -\frac{1}{2} \left[b_z^2 + \left(\frac{\lambda_p n_p + \lambda_n n_m}{2 \sin^2 \gamma d} \right)^2 - 1 \right] \tag{S27}$$

which can be satisfied by tuning the input angles.

To develop a three-color solution for 465 nm, 635 nm, and 532 nm, we apply both approaches described above. First, we take advantage of $465 \times 4 \approx 635 \times 3$ to nearly overlap these diffraction orders. Somewhat closer overlap between the red and blue diffraction orders can be obtained if 473 nm is used instead of 465 nm. Next, we take advantage of the $n = -4$ diffraction order of the 532 nm light using the "off" state mirrors. Eqs. S26 and S27 show the 465 nm and 532 nm outputs overlap at the out-of-plane position $(b_x, b_y) = (0.399, 0.011)$, which is $(\theta_x^b, \theta_y^b) \sim (23.49°, -0.72°)$. A similar observation has been made in [5], but without the benefit of a closed form solution.

Four-color operation can be realized using a similar approach, taking advantage of the near overlap between the 405 nm -4th and 532 nm -3rd diffraction orders and keeping the 465 nm 4th and 635 nm 3rd diffraction orders. Here, solving eq. S27 for the overlap of the 532 nm and 465 nm, we find $(b_x, b_y) = (0.177, 0.581)$ or $(\theta_x^b, \theta_y^b) \sim (12.54°, \sim 36.15°)$. We illustrate this solution and the set of all joint solutions of the blaze and diffraction conditions for 405 nm, 465 nm, 532 nm, and 635 nm in Fig. S2.

These solutions are promising for improved 3- and 4-color operation, but they require a substantially more complicated mounting structure for the DMD. Because the deviation from the blaze condition for our chosen 3-color configuration leads to negligible degradation of the SIM pattern, we believe it is a superior compromise. For achieving 4-color operation, working with a more complicated experimental configuration may be unavoidable. However, using more extreme angles poses other problems in the optical setup, in particular the tilt of the DMD may exceed the depth of field of the first imaging lens (Supplemental Note 9).
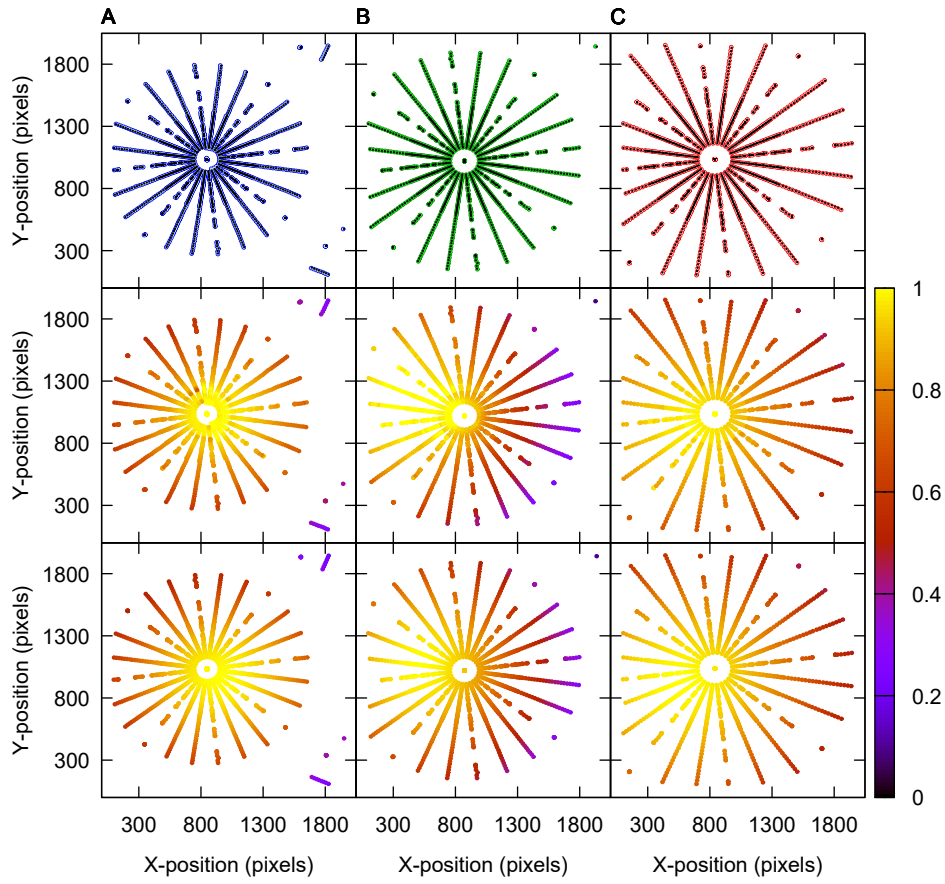
Fig. S3. Model validation Comparison between Fourier peaks measured in the imaging system pupil and the DMD and SIM pattern forward models. **A**. Comparison of measured positions (colored circles) and theoretical positions (black symbols) for nominal wavelengths 465 nm (left), 532 nm (middle), and 635 nm (right). **B**. Measured intensity values across the pupil normalized by the DC value and corrected for the expected diffraction intensity for each frequency component. **C**. Theoretical intensity values across the pupil.

quantity	fit value	expected value
λ_1	464.93 nm	465 nm
$\hat{\mathbf{b}}_1$	(0.2524, -0.2584, -0.9325)	(0.2557, -0.2557, -0.9323)
λ_2	532.70 nm	532 nm
$\hat{\mathbf{b}}_2$	(0.2522, -0.2576, -0.9328)	(0.2557, -0.2557, -0.9323)
λ_3	635.84 nm	635 nm
$\hat{\mathbf{b}}_3$	(0.2525, -0.2587, -0.9324)	(0.2557, -0.2557, -0.9323)
M	31 001	30 769
θ_c	50.05°	—
$\hat{\mathbf{p}}$	(0.2524, -0.2582, -0.9325)	(0.2557, -0.2557, -0.9323)
(c_x, c_y)	(853.9, 1029.4)	—
θ_n	44.47°	45°
d_x	7.598 μm	7.56 μm
d_y	7.558 μm	7.56 μm
w_x	7.598 μm	—
w_y	7.558 μm	—
γ_{on}	12.05°	12°
γ_{off}	−11.96°	−12°

Table S1. DMD parameters determined by non-linear least squares fit.

3. DMD MODEL VALIDATION

To validate the DMD and SIM pattern formation forward models presented in eqs. 1, 5, and 11 of the main text we measure the light diffracted by the DMD for 360 sinusoidal SIM patterns with variable frequency, constructed as described in Supplemental Note 6, and compare the resulting diffraction order positions and intensities to our model. To accomplish this, we place a sCMOS camera in the Fourier plane following lens L6 (see Supplemental Note 7) and record the intensities of a number of diffraction peaks for the various DMD patterns using three wavelengths, 465 nm, 532 nm, and 635 nm. We parameterize these peaks by the DMD Fourier frequency, $\mathbf{f}$, which generates them and perform Gaussian fits to the resulting image to determine their positions, $\mathbf{r}_c^e(\mathbf{f}) = (x_c^e(\mathbf{f}), y_c^e(\mathbf{f}))$ and intensities, $I^e(\mathbf{f})$ on the camera. We compare these intensities and positions to the expected values based on our forward models.

To perform this comparison, we determine the expected location of the diffraction peaks in camera coordinates, $\mathbf{r}_c = (x_c, y_c)$. We first map the pattern frequencies $\mathbf{f} = (f_x, f_y)$ to output angles characterized by the unit vectors $\hat{\mathbf{b}}(\mathbf{f})$, which according to eq. 5 are given by

$$b_{x,y}(\mathbf{f}) \quad = \quad b_{x,y}^o + \frac{\lambda}{d_{x,y}} f_{x,y}, \tag{S28}$$

where the $\mathbf{f}$ are expressed in inverse number of mirrors and $\hat{\mathbf{b}}_o$ is the primary diffraction order of interest.

To map the output angles to pupil coordinates, we suppose the optical axis of the lens L6 is described by the unit vector $\hat{\mathbf{p}}$. To write the frequency in pupil coordinates, we must project the unit vectors $\hat{\mathbf{b}}(\mathbf{f})$ on the plane orthogonal to $\hat{\mathbf{p}}$. To achieve this, we construct an orthonormal coordinate system defined by $\hat{\mathbf{p}}$, $\hat{\mathbf{x}}_p = (p_z, 0, -p_x)/\sqrt{p_x^2 + p_z^2}$ and $\hat{\mathbf{y}}_p = \hat{\mathbf{p}} \times \hat{\mathbf{x}}_p$. Then the diffracted order positions in pupil coordinates are given by $\hat{\mathbf{x}}_p \cdot \hat{\mathbf{b}}(\mathbf{f})$ and $\hat{\mathbf{y}}_p \cdot \hat{\mathbf{b}}(\mathbf{f})$.

Finally, the camera coordinates are related to the pupil coordinates by an affine transformation

with no shear

$$
\begin{pmatrix} x_c(\mathbf{f}) \\ y_c(\mathbf{f}) \\ 1 \end{pmatrix} = M \begin{pmatrix} \cos\theta_c & -\epsilon\sin\theta_c & c_x \\ \sin\theta_c & \epsilon\cos\theta_c & c_y \\ 0 & 0 & 1 \end{pmatrix} \begin{pmatrix} \hat{\mathbf{x}}_p \cdot \hat{\mathbf{b}}(\mathbf{f}) \\ \hat{\mathbf{y}}_p \cdot \hat{\mathbf{b}}(\mathbf{f}) \\ 1 \end{pmatrix} ,
\tag{S29}
$$

where $\epsilon = \pm 1$ if the camera coordinates are not inverted (inverted) relative to the pupil coordinates and (c_x, c_y) is the center of the pupil in camera coordinates. The magnification is the ratio of the lens focal length to the camera pixel size, $M = f_l/d_c$.

On the other hand, the intensities in the pupil can be obtained from eq. 4,

$$
I(\mathbf{f}) \propto \mathrm{sinc}^2\left[A_+\left(\gamma, \hat{\mathbf{a}} - \hat{\mathbf{b}}(\mathbf{f}), \hat{\mathbf{n}}\right)\right] \mathrm{sinc}^2\left[A_-\left(\gamma, \hat{\mathbf{a}} - \hat{\mathbf{b}}(\mathbf{f}), \hat{\mathbf{n}}\right)\right]
\tag{S30}
$$

$$
A_+ = \begin{pmatrix} n_x^2(1-\cos\gamma) + \cos\gamma \\ n_x n_y(1-\cos\gamma) + n_z\sin\gamma \\ n_x n_z(1-\cos\gamma) - n_y\sin\gamma \end{pmatrix} \cdot \left(\hat{\mathbf{a}} - \hat{\mathbf{b}}\right)
\tag{S31}
$$

$$
A_- = \begin{pmatrix} n_x n_y(1-\cos\gamma) - n_z\sin\gamma \\ n_y^2(1-\cos\gamma) + \cos\gamma \\ n_y n_z(1-\cos\gamma) + n_x\sin\gamma \end{pmatrix} \cdot \left(\hat{\mathbf{a}} - \hat{\mathbf{b}}\right)
\tag{S32}
$$

where we know emphasize the dependence of $A_\pm$ on the mirror rotation angle γ and the rotation axis $\hat{\mathbf{n}}$, and provide expressions for the A's for arbitrary $\hat{\mathbf{n}}$. In the main text, assume $\hat{\mathbf{n}} = (1, 1, 0)/\sqrt{2}$.

This provides a complete model of DMD diffraction. Now, we take wavelength λ_i using diffraction orders $(n_i, -n_i)$, some of which rely on "on" mirror angles γ_{on} and some which rely on the "off" mirror angles γ_{off}. Three sets of parameters must be determined: those related to the beam angles $\{b_x(\lambda_i), b_y(\lambda_i), \lambda_i\}$, the pupil mapping $\{M, \theta_c, p_x, p_y, c_x, c_y\}$, and the DMD parameters $\{\theta_n, d_x, d_y, w_x, w_y, \gamma_{\text{on}}, \gamma_{\text{off}}\}$. Here θ_n parameterizes the in-plane rotation of the DMD mirror rotation axis $\hat{\mathbf{n}}$, as we suppose $n_z = 0$. These are supplemented by the known values $\eta_i = \pm 1$ if the diffraction of interest comes from the "on" or "off" mirror state.

Many of these parameters are known to a reasonable degree of accuracy, but to find the best match between this model and the experimental data we perform a non-linear least squares fit using the cost function

$$
\begin{aligned}
C &= \sum_{f,i} \alpha \left([x_c(\mathbf{f}) - x_c^e(\mathbf{f})]^2 + [y_c(\mathbf{f}) - y_c^e(\mathbf{f})]^2\right) \\
&+ \left(\frac{I^e(\mathbf{f})}{I^e(0)} \bigg/ \left|\frac{E(\mathbf{f})}{E(0)}\right|^2 - \mathrm{sinc}^2\left[A_+\left(\gamma_i, \hat{\mathbf{a}} - \hat{\mathbf{b}}_i(\mathbf{f}), \hat{\mathbf{n}}\right)\right] \mathrm{sinc}^2\left[A_-\left(\gamma_i, \hat{\mathbf{a}} - \hat{\mathbf{b}}_i(\mathbf{f}), \hat{\mathbf{n}}\right)\right]\right)^2
\end{aligned}
\tag{S33}
$$

where $\gamma_i = \gamma_{\text{on/off}}$ for $\eta_i = \pm 1$. Here the $E(\mathbf{f})$ are the predictions for the diffracted order strengths given by eq. 11. The parameter α weights the relative contributions of the position and intensity data and is set empirically to 1×10^{-3}, a value that achieves a reasonable balance between the position and amplitude cost functions. Changing α by an order of magnitude has a weak effect on the obtained parameter values.

Minimizing this cost function, we find excellent agreement between the theory and experimental results, shown in table S1. The high quality agreement between the experiment and theory results validates the models presented in the main text.

Note that the pupil mapping model described here has important consequences for the diffraction pattern in the system Fourier plan. Due to the tilted DMD, the ± 1 diffraction orders are not perfectly symmetric about the center of the Fourier plane and are not perfectly colinear with the 0th order. This previously unconsidered effect changes the position of the diffraction orders by up to $\sim 10\%$ compared with naive predictions and must be considered when designing high quality Fourier masks.

4. DMD DIFFRACTION EFFICIENCY

The DMD, like all binary diffractive optics, has relatively low diffraction efficiency, which requires use of high power lasers to illuminate a large FOV. Still, the blazed grating effect allows more efficient coupling into a single diffraction order compared with ferroelectric LCoS SLM's. We expect the peak diffraction efficiency using the all "on" pattern is about 0.91, computed by summing the sinc envelope for all allowed diffraction orders. This efficiency is reduced to ~ 0.69 by reflections from the uncoated DMD window, the finite micromirror reflectivity, and the micromirror fill factor. When the DMD displays the SIM pattern, we expect a fraction of $0.076 \times 0.92 = 0.070$ of this power is diffracted into each of the $\mathbf{f} = \pm \mathbf{f}_o$ orders, where the first factor comes from the diffraction efficiency of the SIM pattern (i.e. eq. 11 in the main text), and the second from the Blaze envelope. This implies an overall efficiency of ~ 0.097. We confirm these estimates in the experiment, where we measure an efficiency of 0.60 for the all "on" pattern using Gaussian beams with small waists compared to the DMD size. Using our typical experimental configuration, these efficiencies are further reduced by a factor of ~ 2 because the beam overfills the DMD aperture to create a more uniform illumination profile. In this configuration, we find the efficiency is ~ 0.3 for all "on" and ~ 0.04 and for the two SIM beams.

The efficiency of the light transfer is further limited by polarization effects and the finite efficiency of the polarization optics. Unpolarized light passing through the pizza polarizer reduces the efficiency by another factor of 0.5, and the transmission efficiency of the polarizer reduces it by 0.5–0.9, with lower transmission in the blue and higher in the red. Thus, the net efficiency of the entire optical train is ~ 0.01–0.02.

5. DMD ABERRATIONS
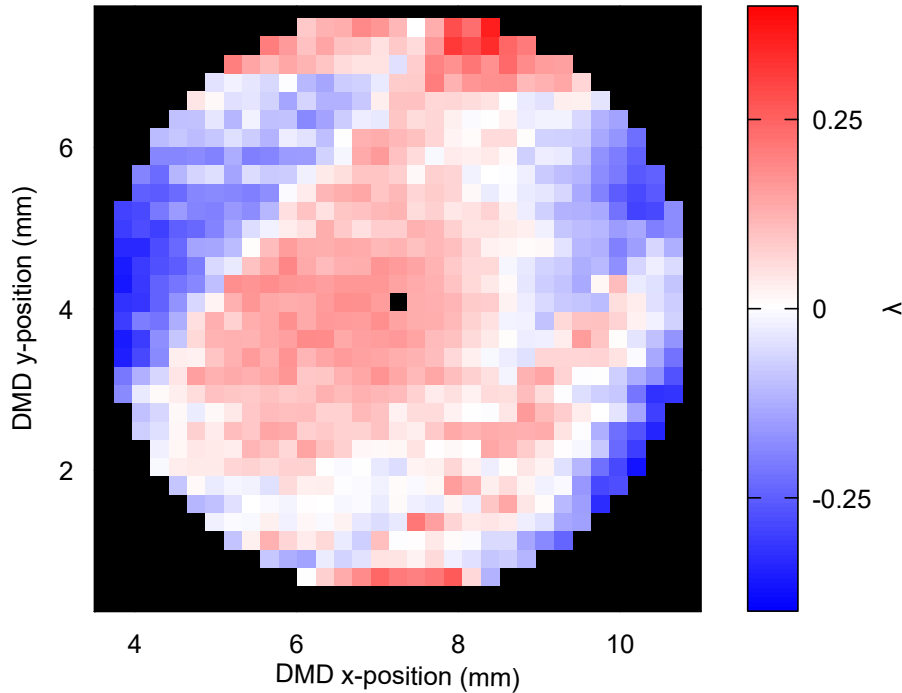
Fig. S4. Experimental DMD aberration measurement. DMD aberration profile over a radius of 3.44 mm, or 475 micromirrors. The DMD flatness is roughly $\lambda/2$ over this range, measured at $\lambda = 780$ nm.

There is anecdotal evidence that DMD's are not optically flat, leading to more aberrations and limiting the utility of DMD's compared with LCoS SLM's. To experimentally characterize the DMD flatness, we adopted the approach of [6]. We considered a circular region near the center of our DMD with radius 3.44 mm, and used sets of patterns with two patches of active mirrors, each

with radius 10 mirrors. Light diffracted from two spots interferes in the Fourier plane, and the phase of the interference pattern contains information about the DMD aberrations. We utilized spot patterns generated from SIM patterns with $\mathbf{r}_1 = (-15, 26)$ and $\mathbf{r}_2 = (-6, 6)$ and period 2.2 mirrors. We sampled the DMD at 1088 points, which required 5441 distinct DMD patterns. At each point we imaged three patterns identical except for $2\pi/3$ phase shifts of the sample patch and two patterns with only one active spot for amplitude normalization. Our results are shown in fig. S4, where we find that over this range the DMD flatness is roughly $\lambda/2$ at 780 nm. For this measurement, we used a 780 nm laser coupled through a single mode optical fiber and diffracting from the "off" DMD mirrors using the $(-3, 3)$ diffraction order.

One source of the relative robustness of our system to DMD aberrations is the fact the DMD is in a conjugate plane to the sample. Here, the structured light patterns are mostly sensitive to local aberrations on the scale of one unit cell, while the DMD primarily has aberrations on the full chip scale. This is the opposite case from [6], where the DMD was placed in a Fourier plane. They found it necessary to correct for the DMD aberrations because local information from the imaging plane is spread across the Fourier plane, and hence experiences the full aberration profile.

The main effect of DMD aberrations, as illustrated in Fig. 3 of the main text, is to broaden the diffraction orders, but there are various other potential sources of diffraction order broadening. DMD aberrations will be the most important limitation to system performance only when they are the dominate source of broadening. Even in an ideal system, some broadening is expected from the finite size of the DMD chip and the numerical aperture of the detection lenses. The finite angle between the DMD normal and the optical axis results in a small amount of defocus which will lead to broadening. Any deviations from a flat wavefront on the DMD will also lead to broadening. A non-flat wavefront can be caused by either the DMD chip not being flat, the window protecting the DMD not being flat, or the incident beam wavefront not being flat. Incomplete temporal or spatial coherence of the light source will lead to a similar effect, due to incomplete interference in the Fourier plane. For example, imaging the DMD with a completely incoherent light source will not produce discrete diffraction orders in the Fourier plane.

In our system, the dominate source of broadening is most likely the limited spatial coherence of the laser sources after coupling through the multimode fiber. For the measured DMD aberration profile, we expect the diffraction order standard deviation is less than 50 μm, whereas we measure diffraction orders of standard deviation ~250 μm. Tests with single mode lasers show reduced diffraction order size, supporting this claim.

We achieve high modulation contrast in our SIM patterns despite the measured DMD and laser non-idealities.

6. MULTICOLOR PATTERN GENERATION ALGORITHM

wavelength	$\mathbf{r}_1$	$\mathbf{r}_2$	P	θ
465/473 nm	(-3, 11)	(3, 12)	6.05	15.26°
	(-11, 3)	(12, 3)	6.05	74.74°
	(-13, -12)	(12, 3)	5.93	132.71°
532 nm	(-3, 11)	(3, 15)	6.84	15.26°
	(-11, 3)	(15, 3)	6.84	74.74°
	(-13, -12)	(3, 12)	6.78	132.71°
635 nm	(-5, 18)	(-15, 24)	8.03	15.52°
	(-18, 5)	(-24, 15)	8.03	74.48°
	(-11, -10)	(15, 3)	7.87	132.27°

Table S2. Parameters of the DMD SIM patterns produced by the multicolor pattern generation algorithm. Note that the 473 nm patterns are also used for the 465 nm laser in the experiment.

We developed an algorithm to identify multicolor SIM patterns for an arbitrary number of wavelengths. The inputs to this algorithm are the approximate period of the desired SIM patterns, P, at one wavelength, the number of different angles, $n_a \geq 3$, the desired number of phases

per pattern n_p and a set of wavelengths λ_i. The criteria the patterns must satisfy are (1) the angles must be close to equally spaced by π/n_a, (2) the periods of patterns for different angles must match to good precision, (3) no parasitic Fourier modes from one pattern should overlap with the main frequency of another, and (4) patterns for different colors but the same angle must pass through the same location in the Fourier plane, which implies $P(\lambda_1)\lambda_1 = P(\lambda_2)\lambda_2$. Unlike previous implementations our pattern generation algorithm does not rely on exhaustive generation of lattice vectors [7].

Given a period P and angle θ, an algorithm to generate a single pattern must produce $\mathbf{r}_{1,2}$ such that $\mathbf{k}_2$ lies at angle θ and $1/|\mathbf{k}_2| = P$. Further, the imposed form of $\mathbf{r}_2 = (n, m)n_p$ constrains the reciprocal lattice vectors

$$\mathbf{k}_1 \quad = \quad \frac{1}{mr_{1x} - nr_{1y}}(m, -n) \tag{S34}$$

$$\mathbf{k}_2 \quad = \quad \frac{1}{n_p(mr_{1x} - nr_{1y})}(r_{1y}, -r_{1x}). \tag{S35}$$

Since the direction of $\mathbf{k}_1$ is already fixed, our strategy is to choose $1/|\mathbf{k}_2|$ close to the desired period P with the constraint that the components of $\mathbf{r}_1$ must be integers. We must match both the angle and period of $\mathbf{k}_2$, i.e.

$$\theta \quad = \quad \arctan\left(-\frac{r_{1x}}{r_{1y}}\right) \tag{S36}$$

$$P \quad = \quad 1/|\mathbf{k}_2| = n_p\left[n\cos(\theta) + m\sin(\theta)\right] \tag{S37}$$

Our full algorithm generates the complete set of $n_a \times n_p$ patterns at each wavelength. We first describe the algorithm for generating a set of SIM patterns for one wavelength, and then discuss the generalization to multiple wavelengths. We begin by selecting a desired period, number of SIM angles n_a, and number of phase shifts n_p. Then we generate a list of possible angles for integers $n, m < M$ using eq. S37. For each n, m and fixed P, eq. S37 can be rewritten as a quadratic equation in $x = \cos\theta$. From this set of available angles we select sequences of angles $\theta_1 < \theta_2 < ... < \theta_{n_a}$, where the distance between adjacent angles is within a certain tolerance of the ideal spacing, π/n_a. We order our collection of sets of angles by the sizes of the $\mathbf{r}_2$ vectors,

$$C \quad = \quad \sum_{i=1}^{n_a} |\mathbf{r}_2(\theta_i)|. \tag{S38}$$

This is a proxy for choosing a pattern set with well separated parasitic diffraction peaks, as large $\mathbf{r}_2$ vectors result in small reciprocal vectors.

For a given sequence of angles, we choose candidates for the vectors $\mathbf{r}_1$. For each angle, we generate $\mathbf{r}_1$ options by finding good rational approximations to $\tan\theta = -r_{1x}/r_{1y}$ for $r_{1x}, r_{2x} \in \{0, ..., N\}$. $N \approx 60$ is sufficient to match the desired θ to better than $1°$, which in turn ensures that the actual period P matches the desired period to within a few percent.

We take all rational approximation of the angle within a certain tolerance, and select the set of $\mathbf{r}_1$ that maximize the distance between the SIM peaks and parasitic diffraction orders from other patterns. This is equivalent to maximizing the distance between $\mathbf{r}_2(\theta_i)$, the frequency of each SIM pattern, and all frequencies of each other pattern, which are given by $s\mathbf{k}_1(\theta_j) + t\mathbf{k}_2(\theta_j)$. This distance is given by

$$d_{\min} \quad = \quad \min_{i \neq j}\left[\min_{s,t \in \mathbb{Z}}\left|\mathbf{k}_2(\theta_i) - s\mathbf{k}_1(\theta_j) - t\mathbf{k}_2(\theta_j)\right|\right]. \tag{S39}$$

In practice, we only include reciprocal lattice vectors where the Fourier component of the pattern is nonzero in our minimization. For each angle set, we select the $r_1(\theta_i)$ by maximizing this distance. We select the final pattern by evaluating this for several angle sets.

This procedure is easily extended to multiple colors. When generating patterns for multiple wavelengths, we want to satisfy $P(\lambda_1)\lambda_1 = P(\lambda_2)\lambda_2$. In this case, we generate a set of angles for all wavelengths and specify an angular tolerance $\delta\theta$. For each angle, we check to ensure all wavelengths have an allowed angle within $\delta\theta$, and discard any angles that do not satisfy this constraint. Then, we proceed with the angle minimization routine described above, now taking the minimum pattern separation (scaled by the wavelength) over all colors. The results of this algorithm for a pattern period of ~ 6 mirrors at 473 nm, 532 nm, and 635 nm are shown in Fig. S2.
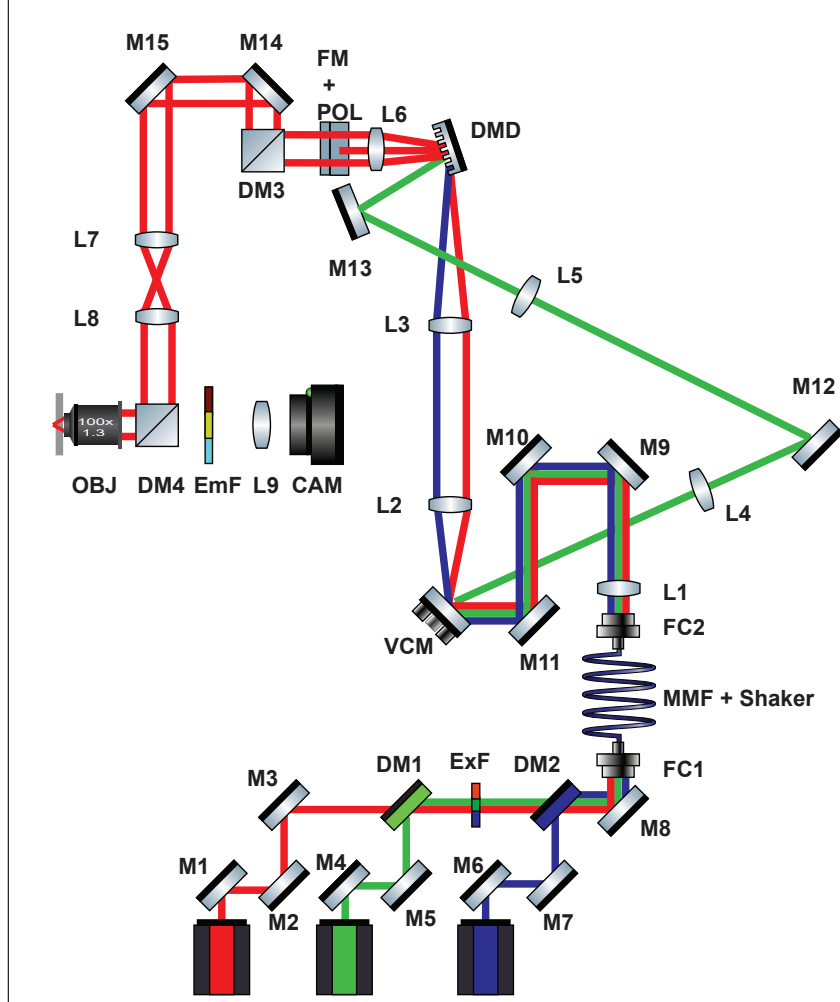
7. SIM INSTRUMENT DESIGN

Fig. S5. Schematic of microscope optical train. Components of the three-color DMD microscope, corresponding to the parts described in table S3.

One objective of our design was to enable ease of use and to minimize effort needed adopt, modify, and develop new imaging experiments using multiple coherent light sources and a DMD. With this in mind, our multicolor SIM system was assembled entirely from commercially available parts, easily machined or 3D printed parts, and standard optical components.

Coherent light was supplied by diode and diode-pumped solid-state (DPSS) lasers made by Lasever. We utilized a blue laser (either 465 nm or 473 nm), green laser (532 nm), and red laser (635 nm). We used the 473 nm laser (LSR473NL-150) for the two-color fixed cell imaging. We used the 465 nm laser (OEM 470nm-2W) for the OTF measurement, the Argo-SIM slide resolution test, the three-color live-cell imaging, and DMD model validation. Although the nominal wavelength of the OEM 470nm-2W laser is 470 nm, we estimate its actual wavelength is ∼465 nm based on the transmitted fraction of light from a dichroic mirror with sharp edge in the blue. This wavelength is confirmed by the model fit in Supplemental Note 3. The various colors were combined with dichroic mirrors (M1-8, DM1, DM2) and coupled into a square-core multimode optical fiber with core size 150 μm (MMF) using a reflective coupler (FC1). The fiber was shaken using an agitator module [8] to reduce the influence of speckle.

The output from the fiber (FC2) was imaged onto the surface of a dual-axis voice-coil mirror (VCM) using an $f = 30$ mm achromat (L1). A voice-coil mirror was used because of the large mirror area (15 mm) compared to standard available galvonometer mirrors. The surface of the

Table S3. Optical elements

Component	Supplier	Part number	Description
Blue laser	Lasever	LSR473NL-150	
Blue laser	Lasever	OEM 470nm-2W	actual wavelength ~465 nm
Green laser	Lasever	LSR532NL-500	
Green laser	Lasever	LSR532H-2W	
Red laser	Lasever	LSR635-500	
M1-M13	Thorlabs	BB1-E02 / BB2-E02	
DM1	Semrock	LM01-552-25	
ExF	Semrock	LF405-488-532-635-B-OMF	
DM2	Semrock	LM01-480-25	
FC1	Thorlabs	RC02FC-P01	
MMF	Thorlabs	M103L05	
Fiber shaker	Custom	—	Ref [8]
FC2	Thorlabs	SM1FC	
L1	Thorlabs	AC254-30-A-ML	
VCM	Optotune	MR-15-30	
L2	Thorlabs	CLS-SL	
L3	Thorlabs	AC508-400-A-ML	
L4	Thorlabs	AC254-075-AB-ML	
L5	Thorlabs	AC508-500-A-ML	
DMD	Texas Instruments	DLP Light Crafter 6500, DLP6500FYE	
L6	Nikon	MXA20696	
FM	Custom	—	aluminum foil $6\times$ ~1 mm diameter holes
POL	Codixx	colorPol vis 500 BC4 CW01	six element "pizza" polarizer
DM3	Chroma	zt473/532/633rdc-uf3	
L7	Thorlabs	AC508-400-A-ML	
L8	Thorlabs	AC508-300-A-ML	
DM4	Chroma	zt473/532/633rdc-uf3	
EmF	Semrock	LF405-488-532-635-B-OMF	
EmF	Chroma	ZET457NF	
OBJ	Olympus	UPlanFL N 100x, na $= 1.3$	
Objective piezo	Mad City Labs	Nano F-200S	
Sample stage	Mad City Labs	MicroDrive MCL-μD1803	
L9	Olympus	SWLTU-C	
CAM	Hamamatsu	Orca Flash4.0 v2 C11440	

voice-coil mirror was imaged onto a DMD using a scan lens (L2) and an $f = 400$ mm achromat (L3). The DMD was imaged onto the sample plane using a series of two $4f$ imaging systems. The first imaging system was formed by a tube lens (L6) and an $f = 400$ mm achromat (L7). After passing through the tube lens, the various SIM orders were linearly polarized in the azimuthal direction using a segmented ("pizza") polarizer placed in the Fourier plane (POL), and unwanted diffraction orders were removed with a home built aluminum foil Fourier mask mounted on a lens tube (FM). The alignment of both is critical, and so we mounted them on XY-stages (Thorlabs, CXYZ-1 and Thorlabs, CXY2). The second imaging system was formed by an $f = 300$ mm achromat (L8) and the objective lens (OBJ). Before passing through the objective, the incoming light was filtered and reflected off a dichroic mirror (DM4). The emitted fluorescence light passed through the dichroic mirror and additional filters (DM4, EmF) and was imaged onto the camera (CAM) using a tube lens (L9). To improve SIM interference contrast, we use two matched dichroic mirrors (DM3, DM4) placed at a right angle to each other in the system. This is intended to counteract the differential phase shift of a single dichroic on the *s*- and *p*-polarization components of the SIM excitation light [7]. The microscope body was an Olympus IX71 with the factory excitation paths and sample stages removed. 3D sample manipulation was achieved using a motorized XY-stage (Sample stage) and a piezo Z-stage (Objective piezo).

Our goal for ease of use extends to the control and reconstruction software. We created a control scheme that runs underneath the open-source project Micromanager 2.0 Gamma [9] and used a low-cost digital triggering device (Advanced Research Consulting Triggerscope 3B). The experiment was controlled using a desktop computer (Lenovo, ThinkServer TS140) running Microsoft Windows 10 Pro with the software Micro Manager 2.0 Gamma through the BeanShell scripting interface. Users set up multi-dimensional acquisitions as normal in Micromanager 2.0 Gamma and then ran our custom script to execute SIM imaging. This custom script bypassed the standard Micromanager acquisition engine. Instead, we only utilized the Micromanager ring buffer to acquire frames from the camera and the rest of the acquisition is hardware controlled. TTL triggering of the DMD and lasers as well as analog control of the voice coil mirror and objective piezo was accomplished with microsecond timing using the Arduino Due based Triggerscope with custom firmware. The DMD was controlled over USB using custom Python software. The SIM patterns were preloaded on the DMD firmware using the Texas Instruments DLP LightCrafter 6500 and 9000 GUI 4.0.1. We hope future development in this area continues to push towards making high-speed, deterministic hardware triggered microscopy widely available [10].

All instrument control code is available on GitHub (Code 1 [11]).

8. SIM MODULATION CONTRAST

We assess the modulation contrast achieved in our experiment by collecting SIM images of diffraction limited beads on a coverslip. We automatically identify beads, and fit them to Gaussian point spread functions to extract their amplitude. Let A_{ij} be the amplitude extract for a given bead at angle index i and phase index j. Then the modulation depth of the pattern at this position and angle is

$$m_i = \frac{\sqrt{2}}{3} \sqrt{(A_{i1} - A_{i2})^2 + (A_{i2} - A_{i3})^2 + (A_{i3} - A_{i1})^2} / (\sum_j A_{ij}/3). \tag{S40}$$

We typically work with beads with $R = 50$ nm for 465 nm and 532 nm or $R = 100$ nm for 635 nm, which are a substantial portion of the diffraction limit. This modifies the observed modulation depth. To correct for finite bead size, we assume a spherical bead with radius R. For a given SIM pattern with frequency f the total signal from one diffraction-limited bead is given by

$$A(\phi, R, f) = \int_{r<R} \frac{1}{2} \left[1 + m \cos\left(2\pi f x + \phi\right)\right] \, dr^3 / V \tag{S41}$$

$$= \int_{-R}^{R} \pi \left(R^2 - x^2\right) \frac{1}{2} \left[1 + m \cos\left(2\pi f x + \phi\right)\right] \, dx / V \tag{S42}$$

$$= 1 + m \left[\frac{3}{u^3} \left(\sin u - u \cos u\right)\right] \cos\phi \tag{S43}$$

where $u = 2\pi R f$ and $V = \frac{4}{3}\pi R^3$.

So we see the only effect of the finite size of the bead is to modify the measured modulation depth. Thus, dividing the modulation depth obtained from eq. S40 by the expression in brackets in eq. S43 yields the true modulation depth.

For $R = 50$ nm beads near 465 nm and 532 nm, this is a $\sim$10 % effect. For $R = 100$ nm beads at 635 nm, this is a $\sim$30 % effect. Typical average modulation contrasts obtained over hundreds of beads are 0.5, 0.7, and 0.8 for 465 nm, 532 nm, and 635 nm.

9. EFFECT OF DMD TILT

In our setup, the DMD normal is tilted about $\theta_{\mathrm{obj}} = 21.2°$ from the optical axis. This may introduce a spatially varying focal shift across the microscope field of view. The imaging system formed by lenses L6-L8 and the objective images this tilted plane onto the sample plane with a lateral magnification of $M_l = 0.012$. The axial magnification is given by $M_a = n_i M_l^2 = 0.000\,216$, where $n_i = 1.5$ is the index refraction of the immersion oil. This implies (Scheimpflug principle) that the tilt angle in the imaging plane is

$$\theta_{\mathrm{im}} \quad = \quad \arctan\left[\frac{M_a}{M_l}\tan\theta_{\mathrm{obj}}\right], \tag{S44}$$

which in our system is 0.4°.

The image of the DMD thus changes axial position by at most 0.7 μm across our field of view, which is similar to the detection optical system depth of focus, $d = \frac{\lambda n_i}{\mathrm{NA}^2} = 0.56$ μm at $\lambda = 635$ nm.

However, the depth of focus of the detection system is not the relevant parameter. This should actually be compared against the depth of focus of SIM pattern. Due to the coherent nature of the imaging, this may be considerably larger than for an incoherent imaging system.

It would be desirable to arrange the DMD so that its face were normal to the optical axis, however such a configuration cannot be achieved for a generic wavelength. Among the wavelength considered here, fig. S2 demonstrates this would only be approximately possible for 532 nm.

10. SAMPLE PREPARATION

A. Commercial samples for instrument characterization

Fluorescent DNA origami with localized fluorophores separated by 120 nm were used to quantify the initial alignment, point spread function (PSF), and SIM performance (Gattaquant DNA Nanotechnologies STED 120R). Additional calibration was done during alignment using multicolor fluorescent microspheres (Thermo Fisher T14792). A fluorescent slide with patterns intended to evaluate instrument resolution was used to characterized and fine tune SIM performance (Argolight Argo-SIM). A commercial slide with bovine pulmonary arotic endothelial (BPAE) cells labeled for nuclei (DAPI), F-actin (Phalloidin - Alexa488), and mitochondria (MitoTracker Red CMXRos) was used to evaluate and fine tune initial multiple wavelength performance (Thermo Fisher F36924).

B. Live adenocarcinoma epithelial cells

MDA-MB-231, human breast adenocarcinoma, cells (ATCC HTB-26) were cultured on 50 mm diameter #1.5 glass bottomed cell culture dishes (World Precision Instrument, FD5040100) at 37 °C in L-15 Medium (ATCC, 30-2008) with 10 % FBS (ATCC, 30-2020) and 5 % CO2 for a minimum of 24-36 hours to allow for adherence and acclimation. Live cells were then stained for 30 min at 37 °C in 5 mL L-15 medium + 10 % FBS with 100 nM MitoTracker Green FM, 2x CellMask Actin Orange Tracking Stain (Invitrogen, 2212429) and 100 nM LysoTracker Deep Red (Invitrogen, L12492). Stain and medium were aspirated off and replaced with 1 mL–2 mL fresh L-15 + 10 % FBS medium. Stained cells were maintained for a short period of time in a 37 °C incubator until imaging.

11. SIM RECONSTRUCTION

To mathematically express the image data obtained from a single raw SIM image with pattern having spatial frequency $\mathbf{f}_\theta$, angle θ, and phase ϕ, we use the following model

$$D_{\theta,\phi}(\mathbf{r}) \quad = \quad \left[P_{\theta,\phi}(\mathbf{r})O(\mathbf{r})\right] \otimes h(\mathbf{r}) + N_{\theta,\phi} \tag{S45}$$

$$P_{\theta,\phi} \quad = \quad A_{\theta\phi}\left[1 + m_\theta \cos\left(2\pi\mathbf{r}\cdot\mathbf{f}_\theta + \phi\right)\right], \tag{S46}$$

where the $A_{\theta\phi}$ are the amplitudes of the various patterns, the m_θ are the pattern modulation depths (which approach 1 in the ideal case), the $N_{\theta,\phi}$ are the measurement noise for each image, and h is the (intensity) point-spread function of the detection imaging system.

In 2D SIM, 3 angles and 3 phases is sufficient to reconstruct the data naively. In this case, we can use the form of $P_{\theta,\phi}$ to simplify the forward model (eq. S45), if we neglect the noise terms. We find

$$
\begin{pmatrix} D_{\theta,\phi_1}(\mathbf{f}) \\ D_{\theta,\phi_2}(\mathbf{f}) \\ D_{\theta,\phi_3}(\mathbf{f}) \end{pmatrix} = \begin{pmatrix} A_{\phi_1} & 0 & 0 \\ 0 & A_{\phi_2} & 0 \\ 0 & 0 & A_{\phi_3} \end{pmatrix} \begin{pmatrix} 1 & \frac{1}{2}e^{i(\phi_1-\phi_\theta^g)} & \frac{1}{2}e^{-i(\phi_1-\phi_\theta^g)} \\ 1 & \frac{1}{2}e^{i(\phi_2-\phi_\theta^g)} & \frac{1}{2}e^{-i(\phi_2-\phi_\theta^g)} \\ 1 & \frac{1}{2}e^{i(\phi_3-\phi_\theta^g)} & \frac{1}{2}e^{-i(\phi_3-\phi_\theta^g)} \end{pmatrix}
$$

$$
\times \begin{pmatrix} 1 & 0 & 0 \\ 0 & m_\theta e^{i\phi_\theta^g} & 0 \\ 0 & 0 & m_\theta s e^{-i\phi_\theta^g} \end{pmatrix} \begin{pmatrix} O(\mathbf{f})h(\mathbf{f}) \\ O(\mathbf{f}-\mathbf{f}_\theta)h(\mathbf{f}) \\ O(\mathbf{f}+\mathbf{f}_\theta)h(\mathbf{f}) \end{pmatrix}, \tag{S47}
$$

where we have factored out the modulation depth and a global phase offset ϕ_θ^g to emphasize that we are free to regard these quantities as part of the transformation matrix or as part of object vector. From the latter point of view, only the phase differences are relevant for the transformation matrix.

To reconstruct the object $O(\mathbf{f})$ We take advantage of the known DMD patterns and the calibrated affine transformation between the DMD and camera planes to estimate the expected SIM patterns. We then estimate these using an optimization routine which determines the best pattern followed by independent routines to estimate the phase and modulation depth similar to [12].

Prior to parameter estimation, we preprocess the data by removing the camera background, estimated from the image histogram. We correct for intensity deviations between different phase images at each angle by matching the histograms using the scikit-image `match_histograms` function. This correction reduces reconstruction artifacts due to power fluctuations of our multimode laser sources.

Our conventional parameter estimation approach is similar to that described in [12]. We use the known affine transformation from the DMD to camera space [13] to select a search region. We find an initial guess by taking the maximum of the cross correlation on a discrete set of points produced by a fast Fourier transform. We refine this selection, optimizing over continuous frequencies using the Fourier shift theorem. The phase and (optionally) amplitudes are estimated together using the correlation minimization method of Wicker [14]. To obtain the modulation depth, we first fit the power spectrum of the sample to an empirical power law form. Then we fit the region near the SIM peak to the same power law, but a different scaling constant. This constant is the modulation depth.

Once the SIM pattern parameters are determined, we invert eq. S47, obtaining

$$
\begin{pmatrix} I_{\theta,0}(\mathbf{f}) \\ m_\theta e^{-i\phi_\theta^g} I_{\theta,1}(\mathbf{f}) \\ m_\theta e^{i\phi_\theta^g} I_{\theta,-1}(\mathbf{f}) \end{pmatrix} = M^{-1} \begin{pmatrix} D_{\theta,\phi_1}(\mathbf{f}) \\ D_{\theta,\phi_2}(\mathbf{f}) \\ D_{\theta,\phi_3}(\mathbf{f}) \end{pmatrix}, \tag{S48}
$$

where the $I_\epsilon(\mathbf{f})$ are essentially the $O(\mathbf{f}-\epsilon\mathbf{f}_\theta)h(\mathbf{f})$ up to the influence of noise. Before obtaining the $D(\mathbf{f})$ from $D(\mathbf{r})$ from a fast Fourier transform, we decompose $D(\mathbf{r})$ into a smooth and periodic part [15], and keep the periodic part. This is an alternative to multiplying $D(\mathbf{r})$ by an apodization function.

We include a global phase factor in eq. S48, as in general there will be some error in our phase determination. We determine and correct this factor before the images are combined. The phase factor can be estimated based on the fact $|I_\theta(\mathbf{f})|$ should be real. Therefore, after shifting the components to the proper positions in Fourier space, we compute

$$
\phi_\theta^g = -\text{angle}\left(\sum_{\mathbf{f}} \mathcal{T}_{\mathbf{f}_\theta} \left[m_\theta e^{-i\phi_\theta^g} I_{\theta,1}(\mathbf{f}) \right] I_{\theta,0}^*(\mathbf{f}) \right) \tag{S49}
$$

Finally, we reconstruct the object using a combination of Wiener deconvolution filters and

weighted averaging

$$O(\mathbf{f}) \quad = \quad \sum_{\theta,\epsilon} \left[\frac{w_{\theta,\epsilon}(\mathbf{f} + \epsilon \mathbf{f}_\theta)}{\sum_{\theta,\epsilon} w_{\theta,\epsilon}(\mathbf{f} + \epsilon \mathbf{f}_\theta) + \eta} \right] e^{i\epsilon \phi_\theta^g} \mathcal{T}_{\epsilon \mathbf{f}_\theta} \left[\frac{h^*(\mathbf{f})}{|h(\mathbf{f})|^2 \left(1 + \frac{1}{w_{\theta,\epsilon}(\mathbf{f})} \right)} I_{\theta,\epsilon}(\mathbf{f}) \right] A(\mathbf{f}), \quad \text{(S50)}$$

where $\epsilon \in \{1, 0, -1\}$ and the weight factors are the signal-to-noise ratio, which is given by

$$w_{\theta,0}(\mathbf{f}) \quad = \quad |h(\mathbf{f})|^2 \frac{S_\theta(\mathbf{f})}{N_\theta} \quad \text{(S51)}$$

$$w_{\theta,\epsilon=\pm 1}(\mathbf{f}) \quad = \quad m_\theta^2 |h(\mathbf{f})|^2 \frac{S_\theta(\mathbf{f} - \epsilon \mathbf{f}_\theta)}{N_\theta}. \quad \text{(S52)}$$

Here A is an apodization function, and $\eta > 0$ is a Wiener filter parameter that attenuates frequency points with low total weight. $\mathcal{T}_{\mathbf{f}_o} g(\mathbf{f}) = g(\mathbf{f} + \mathbf{f}_o)$ is the Fourier translation operator. The first bracketed term represents a weighted average, while the second is a Wiener filter deconvolution.

The signal-to-noise ratio is modeled using the phenomenological approach from [12]. We assume the noise is white, and estimate the noise power by averaging the power spectral density beyond the optical transfer function cutoff frequency,

$$N_{\theta,\epsilon} \quad = \quad \int_{|\mathbf{f}| > f_{\max}} |I_{\theta,\epsilon}(\mathbf{f})|^2 \; d\mathbf{f} / \int_{|\mathbf{f}| > f_{\max}} 1 \; d\mathbf{f}. \quad \text{(S53)}$$

We model the signal power spectral density as a power law, which is appropriate for many biological samples

$$S_\theta(\mathbf{f}) \quad = \quad A^2 |\mathbf{f}|^{-2\alpha}. \quad \text{(S54)}$$

We restrict $0 \le \alpha \le 1.25$, which prevents observed bias towards large exponents in low SNR data.
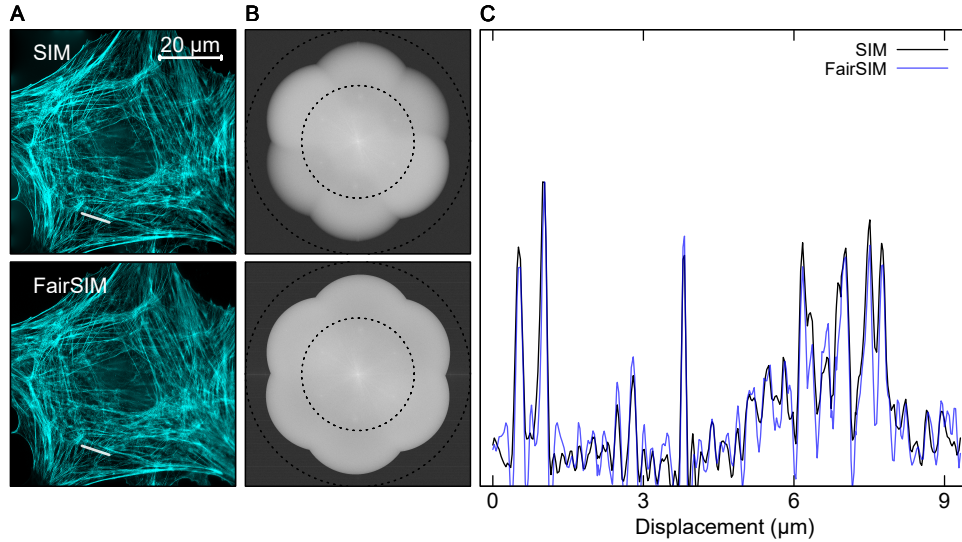
12. COMPARISON OF SIM RECONSTRUCTION WITH FAIRSIM

Fig. S6. Comparison of reconstruction code with FairSIM. A. SIM-SR reconstructions using our reconstruction code (top) and FairSIM (bottom) for the in-focus slice of the BPAE cell images shown in Fig. 6 in the main text. The line cut is illustrated by the semitransparent white line. **B**. Power spectral density of the images in A. **C**. Line cuts through our SIM-SR reconstruction (black) and the FairSIM reconstruction (blue). Each trace is normalized to its peak value. The two reconstruction techniques produce similar results.

To validate our SIM reconstruction algorithm we compare our results with FairSIM [16], a SIM reconstruction program written in Java which has been validated and is commonly used to

reconstruct SIM data [16]. We compare reconstructions of in-focus actin filaments imaged using the 473 nm channel, which are presented in the main text Fig. 6. Prior to performing the FairSIM reconstruction, we preprocess the raw SIM images using the histogram matching procedure described in Supplemental Note 11. We allow FairSIM to generate the OTF using na = 1.3, and attenuation factor $a = 0.3$. We perform the default FairSIM parameter finding routine, and the SIM frequencies it obtains agree with the expected values.

We find our algorithm and FairSIM produce similar reconstructions, each showing similar increase in resolution and corresponding narrowing of filament width (Fig. S6). Because FairSIM uses a different normalization for their SR-SIM data, we first divide the line cut data by the peak value to allow easy comparison. All major features in the line cuts shown in Fig. S6C are present in both, although there are minor differences in smaller features. We also compare the resolution enhancements for the two approaches based on decorrelation analysis. We find that our reconstruction results in an enhancement of 1.54, while theirs yields 1.75 Both the differences in small features and in measured resolution enhancements are most likely due to the different approaches to Wiener filtering used in the two algorithms. These filters have different roll-off characteristics, resulting in different attenuation of high frequency SIM information. Furthermore, our algorithm applies a weighted averaging step which accounts for slightly different SNR's in the SIM images taken at different pattern angles. This effect is visible in the top panel of Fig. S6B, where the frequency information coming from the angle from the upper left to lower right corner is stronger than the other angles. In our reconstruction we use the experimental OTF, and in FairSIM we use their default OTF model. The close agreement in the reconstructed images despite these various implementation differences validates our approach.

13. SIM RECONSTRUCTION OF SYNTHETIC DATA

To further characterize our SIM algorithm and to assess the importance of using the experimentally obtained OTF versus the ideal model, we consider a synthetic filamentous image with features similar to microtubules. Further, this approach allows us to perform reconstruction at a variety of signal-to-noise ratios. This is necessary to fully characterize the SIM reconstruction, as the maximum attainable resolution depends strongly on the SNR value.

To create a synthetic image, we first generate a ground truth image on an oversampled pixel grid. Next, we determine the fluorescence intensity by multiplying this with an illumination pattern and convolving with the point-spread function (PSF) generated from the experimental OTF. Then, we bin the oversampled grid to match the ~60 nm pixel size in our imaging system. We normalize the image so that it has a certain peak photon number, and then we add Poisson noise to each pixel. Next we convert the pixels to camera counts by multiplying by a gain factor of $g = 2$ adu/e and adding an offset of 100 adu, and model camera readout noise by adding Gaussian noise with standard deviation of $\sigma = 4$ adu to each pixel independently. This corresponds to noise of 2 e, similar to the measured rms read noise of our sCMOS camera. We repeat this procedure for all phases and angles to produce synthetic raw SIM data. Finally, we apply the SIM reconstruction algorithm on this simulated image. For each image, we estimate the peak signal-to-noise as

$$\text{SNR} \quad = \quad \frac{g p_{\max}}{\sqrt{g^2 p_{\max} + \sigma^2}}, \tag{S55}$$

where $p_{\max}$ is the peak average photon number incident on any pixel.

To generate the synthetic microtubule images, we first create a ground truth image of 79 one-pixel thick lines representing microtubules on a 10 nm × 10 nm pixel grid with full size 20.46 μm × 20.46 μm. The lines are generated from a filament network file provided by Super Resolution Simulation (SuReSim) [17]. For simplicity, we ignore the z-coordinate and assume the microtubules are all in the same plane. We illustrate a 6 μm × 6 μm portion of the ground truth, simulated SIM image for one angle and phase, and SIM reconstruction in Fig. S7A, B, and C respectively. We assess the SIM algorithm performance by looking at a line cut through the reconstructed data near a crossing between two microtubules, where the microtubules are separated by 110 nm (Fig. S7).

We find that the SIM reconstruction using the experimental OTF can distinguish the closely spaced microtubules for sufficiently large SNR, but the reconstruction using the ideal OTF cannot (Fig. S7E-H). The similarity between Fig. S7G and H indicates that the reconstruction quality of these two images is no longer limited by SNR. The lower resolution of the ideal OTF reconstruction

is expected because the Wiener deconvolution does not correctly reweight the high frequency information in Fourier space. This demonstrates that using an experimentally determined OTF can provide quantitative and qualitative improvement over the ideal OTF.
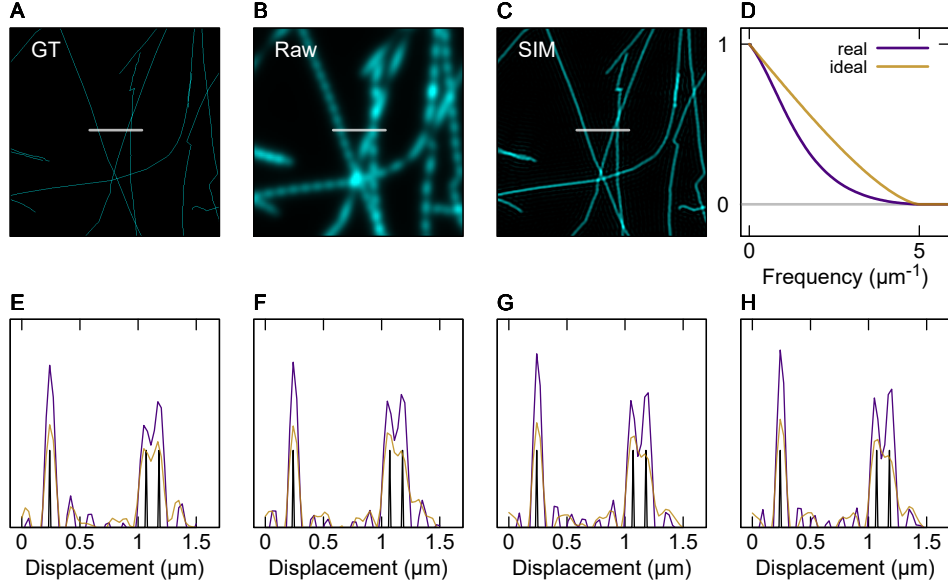

Fig. S7. SIM Reconstruction of synthetic microtubules. A. Ground truth image. Pixels are $10\,\text{nm} \times 10\,\text{nm}$, and the ground truth structures have width of $10\,\text{nm}$. The white line illustrates the location of the line cuts shown in E.-H. **B**. A simulated SIM image with the same signal-to-noise ratio as H. **C**. SIM reconstruction using the experimental OTF for the same SNR as H. **D**. Optical transfer function used to generate the synthetic SIM images (purple) and ideal optical transfer function for na $= 1.3$ and $\lambda = 520\,\text{nm}$ (yellow). **E**. Line cut showing one isolated microtubule (left peak) and two microtubules near a crossing (right peak). The ground truth is shown in black, the SIM reconstruction using the experimental OTF is shown in purple, and the reconstruction using the ideal OTF is shown in yellow. The peak photon number per pixel is $\sim$4000 photons, and peak signal-to-noise ratio is $\sim$60. **F**. As in D. but with SNR $\sim$200 **G**. SNR $\sim$650. **H**. SNR $\sim$2000.

14. OTF MEASUREMENT TECHNIQUE

The forward model for intensity at the imaging plane is the convolution of the electric field predicted by the DMD forward model band limited by the excitation imaging system optical transfer function. The projected intensity components are given by the autocorrelation of this signal, and the final imaged intensity is additionally blurred by the detection system OTF, $H(\mathbf{f})$

$$I(\mathbf{f}) = H(\mathbf{f}) \sum_{\mathbf{s}} \hat{\mathbf{e}}(\mathbf{s}) E(\mathbf{s}) \cdot \hat{\mathbf{e}}(\mathbf{s}-\mathbf{f}) E^*(\mathbf{s}-\mathbf{f}) \ \text{circ}\left(\frac{|\mathbf{s}|}{f_{\max}}\right) \ \text{circ}\left(\frac{|\mathbf{s}-\mathbf{f}|}{f_{\max}}\right) \tag{S56}$$

$$= H(\mathbf{f}) \sum_{\mathbf{s}} \tilde{P}(\mathbf{s}) \tilde{P}^*(\mathbf{s}-\mathbf{f}) \hat{\mathbf{e}}(\mathbf{s}) \cdot \hat{\mathbf{e}}(\mathbf{s}-\mathbf{f}) \ H_{\text{DMD}}(\mathbf{s}) H_{\text{DMD}}^*(\mathbf{s}-\mathbf{f})$$

$$\times \text{circ}\left(\frac{|\mathbf{s}|}{f_{\max}}\right) \ \text{circ}\left(\frac{|\mathbf{s}-\mathbf{f}|}{f_{\max}}\right), \tag{S57}$$

where $\mathbf{f}$ are restricted to the reciprocal lattice vectors of the projected pattern and the $P(\mathbf{f})$ can be obtained from eq. 4. When working with the 473 nm excitation, the corrections from H_{DMD} are $< 10\,\%$ out to the band limit. We neglect possible aberrations in the illumination pupil function, however these could be included in systems where they are relevant. The unit vectors $\hat{\mathbf{e}}(\mathbf{s})$ describe the polarization of the light after diffraction by the imaging system. This equation does not include the typical $\cos^{-1/2}\theta$ apodization factor that appears in the pupil of a system obeying the Abbe sine condition [18], due to the fact that this is a discrete sum and not an integral.

Neglecting H_{DMD}, we have

$$
\begin{aligned}
I(\mathbf{f}) \quad &\approx \quad H(\mathbf{f}) \left[\mathcal{O}(\mathbf{f}) \otimes \sum_{\mathbf{s}} \tilde{P}(\mathbf{s}) \tilde{P}^*(\mathbf{s} - \mathbf{f}) \hat{\mathbf{e}}(\mathbf{s}) \cdot \hat{\mathbf{e}}(\mathbf{s} - \mathbf{f}) \, \mathrm{circ}\left(\frac{|\mathbf{s}|}{f_{\max}} \right) \, \mathrm{circ}\left(\frac{|\mathbf{s} - \mathbf{f}|}{f_{\max}} \right) \right] \quad \text{(S58)} \\
&= \quad H(\mathbf{f}) \left[\mathcal{O}(\mathbf{f}) \otimes \sum_i m(\mathbf{f}_i) e^{i\phi(\mathbf{f}_i)} \delta\left(\mathbf{f} - \mathbf{f}_i \right) \right] \quad \text{(S59)} \\
&= \quad \sum_i H(\mathbf{f}_i) m(\mathbf{f}_i) e^{i\phi(\mathbf{f}_i)} \mathcal{O}\left(\mathbf{f} - \mathbf{f}_i \right). \quad \text{(S60)}
\end{aligned}
$$

If we assume the object is perfectly uniform, this reduces to

$$
\begin{aligned}
I(\mathbf{f}_i) \quad &= \quad \sum_i H(\mathbf{f}_i) m(\mathbf{f}_i) e^{i\phi(\mathbf{f}_i)} \delta(\mathbf{f} - \mathbf{f}_i) \quad \text{(S61)} \\
H(\mathbf{f}_i) \quad &= \quad \frac{I(\mathbf{f}_i)}{m(\mathbf{f}_i) e^{i\phi(\mathbf{f}_i)}}, \quad \text{(S62)}
\end{aligned}
$$

as given by eq. 13 in the main text.

To evaluate the quantities $m(\mathbf{f}_i)$, we must perform the sum above over the known Fourier components of the DMD pattern, and additionally evaluate the polarization vectors. We suppose the $\hat{\mathbf{z}}$ axis coincides with the optical axis, and define unit vectors and input polarization vectors by

$$
\begin{aligned}
\hat{\mathbf{e}}_p \quad &= \quad (\cos\phi, \sin\phi, 0) \quad \text{(S63)} \\
\hat{\mathbf{e}}_s \quad &= \quad (-\sin\phi, \cos\phi, 0) \quad \text{(S64)} \\
\hat{\mathbf{e}}_{\mathrm{in}} \quad &= \quad (\cos\phi_o, \sin\phi_o, 0). \quad \text{(S65)}
\end{aligned}
$$

After diffraction by the optical system, a ray initially incident parallel to the optical axis at azimuthal position ϕ converges towards the focal point and the polarization vector is modified [19]

$$
\begin{aligned}
\hat{\mathbf{e}}_{\mathrm{out}}(\phi, \theta, \phi_o) \quad &= \quad \left(\hat{\mathbf{e}}_p \cdot \hat{\mathbf{e}}_{\mathrm{in}} \right) \hat{\mathbf{e}}_r + \left(\hat{\mathbf{e}}_s \cdot \hat{\mathbf{e}}_{\mathrm{in}} \right) \hat{\mathbf{e}}_s \quad \text{(S66)} \\
\hat{\mathbf{e}}_r \quad &= \quad (\cos\phi \cos\theta, \sin\phi \cos\theta, \sin\theta). \quad \text{(S67)}
\end{aligned}
$$

In this measurement, we work with unpolarized light and hence we must average over the input polarization

$$
\begin{aligned}
\frac{1}{2\pi} \int_0^{2\pi} d\phi_o \, \hat{\mathbf{e}}(\phi_1, \theta_1, \phi_o) \cdot \hat{\mathbf{e}}(\phi_2, \theta_2, \phi_o) = \quad &\frac{1}{2} \cos^2(\phi_1 - \phi_2)\left(1 + \cos\theta_1 \cos\theta_2\right) \\
&+ \quad \frac{1}{2} \cos(\phi_1 - \phi_2) \sin\theta_1 \sin\theta_2 \\
&+ \quad \frac{1}{2} \sin^2(\phi_1 - \phi_2)\left(\cos\theta_1 + \cos\theta_2\right). \quad \text{(S68)}
\end{aligned}
$$

Finally, we must convert between the angular representation used here and the spatial frequency representation discussed above. These are connected by

$$
\mathbf{f} \quad = \quad \frac{n}{\lambda} \left(\cos\phi \sin\theta, \sin\phi \sin\theta \right) \quad \text{(S69)}
$$

In practice, the object fluorescence distribution is not perfectly uniform. This introduces correction terms caused by the same frequency mixing that SIM takes advantage of. The dominant term comes from the object spectrum itself, $H(\mathbf{f})\mathcal{O}(\mathbf{f})$. We can obtain this term directly from a widefield image and subtract it from the measured image. Performing higher order corrections is more challenging, as this requires knowledge of $m(\mathbf{f}_i)\mathcal{O}(\mathbf{f} - \mathbf{f}_i)H(\mathbf{f})e^{i\phi(\mathbf{f}_i)}$, which must be obtained through deconvolution and frequency shifting, similar to SIM reconstruction. To avoid these complications, we choose patterns where the higher order correction terms are unimportant. These patterns typically have large separation between different Fourier peaks, corresponding to large reciprocal lattice vectors and short periods. We find empirically that these corrections are not important for periods less than $\sim$20 mirrors.

Accounting for this effect and additionally dividing measured intensities by their DC component to normalize laser power fluctuations, we estimate the OTF from

$$H(\mathbf{f}) \quad = \quad \frac{1}{m(\mathbf{f})e^{i\phi(\mathbf{f})}} \left[\frac{I_{\text{exp}}(\mathbf{f})}{I_{\text{exp}}(0)} - \frac{I_{\text{widefield}}(\mathbf{f})}{I_{\text{widefield}}(0)} \right]. \tag{S70}$$

In the measurement presented in the main text, we chose 360 SIM patterns at 12 approximately equally spaced angles divided over 180° and 30 different periods equally spaced between 5–20 mirrors. Small deviations from equal spacing are necessary for the patterns to be commensurate with the underlying DMD mirror lattice. We apply a similar algorithm to that described in Supplemental Note 6 to determine these patterns.

To generate an OTF which is convenient to use with the SIM reconstruction algorithm, we empirically model the measured optical-transfer function as a Lorentzian times the ideal optical transfer function generated by the Airy point-spread function,

$$H(\mathbf{f}) \quad = \quad \frac{1}{1 + \gamma^2 |\mathbf{f}|^2} \times H_o(\mathbf{f}). \tag{S71}$$

The Lorentzian attenuates the optical-transfer function at high frequencies. This functional form is convenient because it ensures that the OTF is unity at $\mathbf{f} = 0$, zero at $|\mathbf{f}| = f_{\text{max}}$ and monotonically decreasing. The parameter γ, which controls the width of the Lorentzian, is determined by a non-linear least-squares fit.

This functional form assumes the OTF is azimuthally symmetric which is appropriate here because we find no evidence for a strong angular dependence in the experimental data. Nevertheless, a non-parametric OTF may be determined by smoothing and interpolating the data shown in Fig. 4F for systems which do not possess azimuthal symmetry.

Identifying the SIM peaks efficiently in the camera images requires careful calibration of the affine transformation between the DMD and the camera coordinates, which we obtain by projecting a test pattern of well-separated spots on the DMD, each generated by a single DMD micromirror. We perform Gaussian fits to these spots in the camera image. Additional image markers prevent ambiguities due to reflection and inversion. We then determine the affine transformation using Gaussian elimination.

15. ADDITIONAL SIM EXPERIMENTAL TESTS

A. Gattaquant DNA origami nanorulers

We further assessed the SIM performance on a collection of diffraction limited objects, using Gattaquant DNA origami nanorulers. The nanorulers contain two dye molecules separated by a well defined distance of 120 nm. They are designed for characterizing STED systems, and we did not expect to resolve this small spacing using the 680 nm fluorescence where the maximum theoretical resolution is ∼130 nm. However, the very different characteristics of this sample compared with the fixed cells allowed an independent test of our SIM approach. In these samples the SIM peaks appear weaker due to the smaller DC spatial frequency component as compared with cell samples. However, high frequency content is still efficiently mixed below the band pass, resulting in a large SNR and high-quality reconstruction. As illustrated in Fig. S8, the SIM images show significant narrowing of the individual origami as compared with both the widefield images and deconvolved images. Decorrelation analysis estimates SIM provides a factor of 1.64 resolution enhancement, close to the theoretical maximum based on our pattern spacing. Performing Gaussian fits to ∼2500 DNA origami and comparing the resulting standard deviations for the deconvolved and SIM images gives a similar resolution enhancement estimate of 1.71.
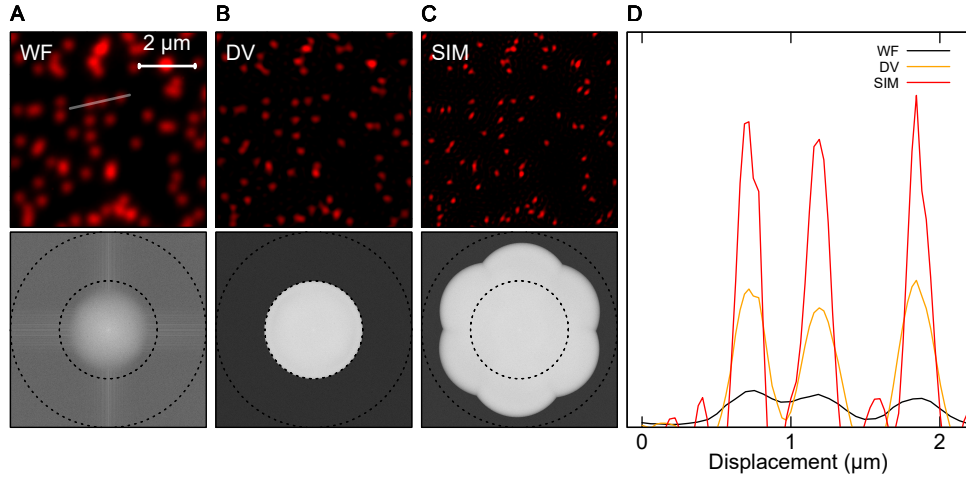
Fig. S8. SIM performance on diffraction limited spots. A. Widefield image for 635 nm (top) and power spectrum (bottom). Images are shown in ADU. Circles illustrate the maximum frequency where the ideal optical transfer function has support for $\lambda_{\text{emission}} = 680$ nm and na $= 1.3$. **B**. Widefield image after Wiener filter deconvolution. **C**. SR-SIM images. **D**. One-dimensional cuts plotted along the lines illustrated in A. We show the widefield image (black line), Wiener deconvolved image (orange), and SR-SIM image (red).

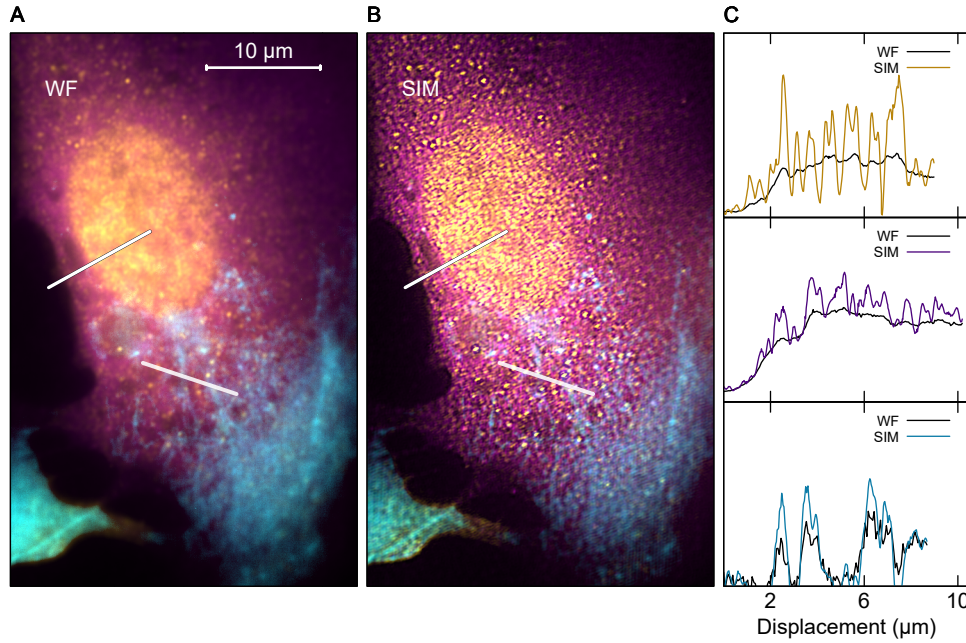## B. Three-wavelength imaging of fixed cells

Fig. S9. Three-color imaging of fixed primary rat endothelial cells. A. Composite widefield image with the 473 nm channel (cyan), 532 nm channel (yellow), and 635 nm channel (magenta). Images are shown in ADU. White lines illustrate the position of the line cut shown in C. **B**. SR-SIM images. **C**. One-dimensional cuts plotted along the lines illustrated in A. for 532 nm (top), 635 nm (middle), and 473 nm excitations. 473 nm and 532 nm channel line cuts correspond to the upper line cut in A., and 635 nm to the lower cut.

We realized three-wavelength SIM using the 473 nm, 532 nm, and 635 nm channels to image

β-actin, HIF, and FGF18 labeled with Alexa Fluor 488, Alexa Fluor 555, and Alexa Fluor 647 in fixed primary rat endothelial cells. We have previously studied angiogenic signaling in primary rat, sheep, and human endothelial cells using high-throughput multi-wavelength widefield microscopy [20–22].

The SIM results (Fig. S9) show resolution enhancement in all three channels, with the enhancement in the details of the HIF distribution from the 532 nm channel appearing most visible in Fig. S9C. Decorrelation analysis estimates the SIM images enhance the resolution over the deconvolved images by by factors of ∼1.6, ∼1.5, and ∼1.65 for the 473 nm, 532 nm, and 635 nm channels respectively.

Primary rat endothelial cells were isolated as previously described [22, 23]. After isolation, cells were plated on glass chamber slides (Thermo Fisher, 177402), fixed using 4 % paraformaldehyde (Electron Microscopy Sciences, 15710-S), and labeled using primary and secondary antibodies for HIF (Primary, 1:250 dilution: Thermo Fisher PA1-184. Secondary, 1:500 dilution, Alexa Fluor 555: Thermo Fisher A32794), β-actin (Primary, 1:1000 dilution: Thermo Fisher AM4302. Secondary, 1:500 dilution, Alexa Fluor 488: Thermo Fisher A-11001), and FGF18 (Primary, 1:250 dilution: Santa Cruz SC-16830. Secondary, 1:500 dilution, Alexa Fluor 647: Thermo Fisher A32849)). After labeling, slides were mounted with Slowfade Glass with DAPI (Thermo Fisher S36920) using 25 mm × 40 mm 1.5 coverslips (Thermo Fisher 24x40-1.5).

REFERENCES

1. D. Dan, M. Lei, B. Yao, W. Wang, M. Winterhalder, A. Zumbusch, Y. Qi, L. Xia, S. Yan, Y. Yang, P. Gao, T. Ye, and W. Zhao, "DMD-based LED-illumination super-resolution and optical sectioning microscopy," Sci. Reports **3** (2013).
2. L. Reymond, J. Ziegler, C. Knapp, F.-C. Wang, T. Huser, V. Ruprecht, and S. Wieser, "SIMPLE: Structured illumination based point localization estimator with enhanced precision," Opt. Express **27**, 24578 (2019).
3. J. E. Harvey and R. N. Pfisterer, "Understanding diffraction grating behavior: including conical diffraction and Rayleigh anomalies from transmission gratings," Opt. Eng. **58**, 1 (2019).
4. A. Sandmeyer, M. Lachetta, H. Sandmeyer, W. Hübner, T. Huser, and M. Müller, "DMD-based super-resolution structured illumination microscopy visualizes live cell dynamics at high speed and low cost," (2019). BioRxiv 10.1101/797670.
5. M. Lachetta, H. Sandmeyer, A. Sandmeyer, J. S. am Esch, T. Huser, and M. Müller, "Simulating digital micromirror devices for patterning coherent excitation light in structured illumination microscopy," Philos. Transactions Royal Soc. A **379** (2021).
6. P. Zupancic, P. M. Preiss, R. Ma, A. Lukin, M. E. Tai, M. Rispoli, R. Islam, and M. Greiner, "Ultra-precise holographic beam shaping for microscopic quantum control," Opt. Express **24**, 13881 (2016).
7. H.-W. Lu-Walther, M. Kielhorn, R. Förster, A. Jost, K. Wicker, and R. Heintzmann, "fastSIM: a practical implementation of fast structured illumination microscopy," Methods Appl. Fluoresc. **3**, 014001 (2015).
8. D. Schröder, J. Deschamps, A. Dasgupta, U. Matti, and J. Ries, "Cost-efficient open source laser engine for microscopy," Biomed. Opt. Express **11**, 609 (2020).
9. A. Edelstein, N. Amodaj, K. Hoover, R. Vale, and N. Stuurman, "Computer control of microscopes using μmanager," Curr. Protoc. Mol. Biol. **92** (2010).
10. R. Chhetri, S. Preibisch, and N. Stuurman, "Software for microscopy workshop white paper," (2020). ArXiv 2005.00082v1.
11. P. T. Brown and D. P. Shepherd, "Qi2lab/mcsim," Https://github.com/QI2lab/mcSIM archived on Zenodo 10.5281/zenodo.4773865.
12. A. Lal, C. Shan, and P. Xi, "Structured illumination microscopy image reconstruction algorithm," IEEE J. Sel. Top. Quantum Electron. **22**, 50–63 (2016).
13. P. Křížek, I. Raška, and G. M. Hagen, "Flexible structured illumination microscope with a programmable illumination array," Opt. Express **20**, 24585 (2012).
14. K. Wicker, O. Mandula, G. Best, R. Fiolka, and R. Heintzmann, "Phase optimisation for structured illumination microscopy," Opt. Express **21**, 2032 (2013).
15. L. Moisan, "Periodic plus smooth image decomposition," J. Math. Imaging Vis. **39**, 161–179 (2010).
16. M. Müller, V. Mönkemöller, S. Hennig, W. Hübner, and T. Huser, "Open-source image

reconstruction of super-resolution structured illumination microscopy data in ImageJ," Nat. Commun. **7** (2016).

17. V. Venkataramani, F. Herrmannsdörfer, M. Heilemann, and T. Kuner, "SuReSim: simulating localization microscopy experiments from ground truth models," Nat. Methods **13**, 319–321 (2016).

18. M. Leutenegger, R. Rao, R. A. Leitgeb, and T. Lasser, "Fast focus field calculations," Opt. Express **14**, 11277 (2006).

19. B. Richards and E. Wolf, "Electromagnetic diffraction in optical systems, II. structure of the image field in an aplanatic system," Proc. Royal Soc. London. Ser. A. Math. Phys. Sci. **253**, 358–379 (1959).

20. M. A. Ahern, C. P. Black, G. J. Seedorf, C. D. Baker, and D. P. Shepherd, "Hyperoxia impairs pro-angiogenic RNA production in preterm endothelial colony-forming cells," AIMS Biophys. **4**, 284–297 (2017).

21. C. Kim, G. J. Seedorf, S. H. Abman, and D. P. Shepherd, "Heterogeneous response of endothelial cells to insulin-like growth factor 1 treatment is explained by spatially clustered sub-populations," Biol. Open **8** (2019).

22. G. Seedorf, C. Kim, B. Wallace, E. W. Mandell, T. Nowlin, D. Shepherd, and S. H. Abman, "rhIGF-1/BP3 preserves lung growth and prevents pulmonary hypertension in experimental bronchopulmonary dysplasia," Am. J. Respir. Critical Care Medicine **201**, 1120–1134 (2020).

23. C. Iosef, T.-P. Alastalo, Y. Hou, C. Chen, E. S. Adams, S.-C. Lyu, D. N. Cornfield, and C. M. Alvira, "Inhibiting nf-κb in the developing lung disrupts angiogenesis and alveolarization," Am. journal physiology. Lung cellular molecular physiology **302**, L1023–36 (2012).